

Performance of a black-box-type rovibrational method in comparison with a tailor-made approach: case study for the methane-water dimer

Alberto Martín Santa Daría,¹ Gustavo Avila,¹ and Edit Mátyus^{1,*}

¹*Institute of Chemistry, ELTE Eötvös Loránd University*

Pázmány Péter sétány 1/A 1117 Budapest, Hungary

(Dated: April 20, 2021)

Abstract

The present work intends to join and respond to the excellent and thoroughly documented rovibrational study of [X.-G. Wang and T. Carrington, Jr., J. Chem. Phys. 154, 124112 (2021)] that used an approach tailored for floppy dimers with an analytic dimer Hamiltonian and a non-product basis set including Wigner D functions. It is shown in the present work that the GENIUSH black-box-type rovibrational method can approach the performance of the tailor-made computation for the example of the floppy methane-water dimer. Rovibrational transition energies and intensities are obtained in the black-box-type computation with ‘only’ 2-3 times larger basis set sizes and in an excellent numerical agreement in comparison with the more efficient tailor-made approach.

* edit.matyus@ttk.elte.hu

I. INTRODUCTION

Electronic structure theory has general program packages that work for n electrons, where n is defined by the user together with the configuration of the clamped nuclei.

Will computational (ro)vibrational spectroscopy methodology reach this level of automatization? Does it need it to reach this and why? One may argue, that careful gas-phase spectroscopy measurements conducted in order to explore the structure and internal dynamics of molecular systems typically assume months or even years of systematic experimental work (development of sample preparation, source and detector architectures, uncertainty estimation, error control, etc.). It is not a typically high-throughput field studying one molecule after the other at an extraordinary pace. At the same time, the experiments may produce large sets of precise data that provide a highly detailed characterization of the quantum dynamical features of the system.

Regarding computational molecular rovibrational spectroscopy, it is a natural aim for a mathematically formulated theory to have an approach, an algorithm, and a computer program that is generally applicable, limited ‘only’ by the available computational resources. For solving the rovibrational Schrödinger equation, it should be an general N -particle approach, where N is the number of atomic nuclei (although, for the moment only finite many N possible values are computationally feasible). In this field, it is another necessary condition to allow the user to specify the internal coordinates and the body-fixed frame best suited for the computations.

Development of Ref. [1], following earlier work in the field [2–6], was led by this idea in spite of the fact that there were already excellent approaches available specifically designed for special types of molecular systems (with a given number of nuclei and specific coordinates), the list includes, for example Refs. [7–15]. The numerical advantage of an N -particle method was not at all obvious over the performance of tailor-made approaches. For semi-rigid systems, the Eckart–Watson Hamiltonian [16] was available as a general N -particle Hamiltonian, and for which efficient solution techniques have been developed using basis pruning [17, 18]. If basis pruning can be efficiently realized, then the grid pruning techniques can be employed [19, 20] to milden the curse of dimensionality. Most recently, basis and grid pruning tech-

niques have been used to describe efficiently the semi-rigid part of floppy complexes in full dimensionality [21–23].

Floppy molecular systems with multiple large-amplitude motions was and (is still) an open challenge for the field, so it was natural to ask the following questions about a novel black-box-type approach. 1) Can the black-box-type rovibrational approach tackle floppy systems? 2) Can we come close in efficiency to tailor-made approaches for floppy systems? Although singular regions can be explored numerically, there are difficulties connected to the selection and use of good basis functions and integration grids without an analytic knowledge of the kinetic energy operator (KEO) and its matrix elements [21]. 3) Is it necessary to group the coordinates in a certain fashion and use specifically coupled basis functions, or is it possible to continue using the simpler direct product basis and grid representations for a start, that can be pruned perhaps at a next stage of the development?

In the present work, we will show for the example of the methane-water dimer that the answer to all three questions, 1–3), is ‘yes’.

We use the methane-water dimer as an example system, because Wang and Carington [24] recently reported and carefully documented their work using a tailor-made dimer Hamiltonian, Wigner D basis functions, and the symmetry adapted Lanczos eigensolver for computing rovibrational transitions of this dimer. They have carefully compared their computational results with earlier black-box-type rovibrational computations carried out for this system [25–27], and pointed out that even an excessively large direct-product basis and grid provided not sufficiently converged rovibrational energies, with inaccuracies on the order of 0.05–1.5 cm^{-1} . Since the publication of the first applications of the GENIUSH program for molecular dimers, we have gathered more experience in treating floppy complexes, and using this development and experience we wish to complement this comparison.

The methane-water dimer is also a chemically and spectroscopically important example. It is the simplest model for water-hydrocarbon interactions, there are high-resolution far-infrared [28] and microwave spectroscopic data [29] available for the system, while the analysis of the congested spectrum was difficult and only partially possible by effective Hamiltonians.

In this work, we will show that using an order of magnitude *smaller* but bet-

ter basis and grid representation, than in earlier work [25–27], we can converge the rovibrational energies to 10^{-3} cm^{-1} with a basis and grid that is ‘only’ 2-3 times larger, than the coupled basis used by Wang and Carrington [24]. The tailor-made approach remains to be more efficient, but not by orders of magnitude. The efficiency of the GENIUSH computation can be further enhanced by exploiting part of the rich symmetry features [30] of this particular complex. We think that the level of convergence achieved in this work is much beyond the range of the typical approximations underlying the current computational rovibrational spectroscopy framework (quality of the potential energy surface, Born–Oppenheimer and non-relativistic approximations).

Finally, we may ask whether we can expect any fundamental or numerical advantage from developing general rovibrational approaches, apart from fulfilling a mathematical ‘necessity’.

First of all, we may aim for automatically defining internal coordinates that are optimal or near optimal for a particular computation (system and energy range).

Furthermore, for a floppy molecular system, a fundamental and numerically important open problem is finding the optimal body-fixed frame, or at least a body-fixed frame that is good enough or better than another one. For small-amplitude vibrations, the Eckart frame is known to be an excellent choice in minimizing the rotational and vibrational problem for low-energy rovibrational states, and thus, it allows us to use the $J = 0$ vibrational eigenfunctions as a basis for $J > 0$ computation [31] in the same energy range. For higher excited semi-rigid systems and especially for floppy systems, we do not have any practical approach for finding a good or at least a ‘better’ frame, and it may be the numerical KEO approach used also in the GENIUSH program that will allow us to optimize the molecular frame ‘on-the-fly’ over a grid [32].

Having this perspective in mind, after a short theoretical introduction (Sec. II), we report rovibrational energies (Secs. III and IV), transitions and line strengths (Secs. V, VI, and VII) for the example of methane-water obtained with the numerical KEO approach of GENIUSH and using the potential energy surface (PES) developed by Akin-Ojo and Szalewicz [33].

II. THEORETICAL DESCRIPTION AND COMPUTATIONAL DETAILS

The quantum dynamical computations were carried out by using the GENIUSH [1, 34] computer program. This program package has been used already to study a number of semi-rigid and floppy molecular systems [21–23, 25–27, 30, 35–40], so here we only shortly summarize the theoretical background. The general rovibrational Hamiltonian [2–6, 41]

$$\begin{aligned}
\hat{H} &= \frac{1}{2} \sum_{k=1}^D \sum_{l=1}^D \tilde{g}^{-1/4} \hat{p}_k G_{kl} \tilde{g}^{1/2} \hat{p}_l \tilde{g}^{-1/4} \\
&+ \frac{1}{2} \sum_{k=1}^D \sum_{a=1}^3 (\tilde{g}^{-1/4} \hat{p}_k G_{k,D+a} \tilde{g}^{1/4} + \tilde{g}^{1/4} G_{k,D+a} \hat{p}_k \tilde{g}^{-1/4}) \hat{J}_a \\
&+ \frac{1}{2} \sum_{a=1}^3 G_{D+a,D+a} \hat{J}_a^2 \\
&+ \frac{1}{2} \sum_{a=1}^3 \sum_{b>a}^3 G_{D+a,D+b} [\hat{J}_a, \hat{J}_b]_+ + \hat{V}
\end{aligned} \tag{1}$$

is implemented in the GENIUSH program. In Eq. 1, \hat{J}_a ($a = 1(x), 2(y), 3(z)$) are the body-fixed total angular momentum operators and $\hat{p}_k = -i\partial/\partial q_k$ with the q_k ($k = 1, 2, \dots, D$) internal coordinates. The $G_{kl} = (\mathbf{g}^{-1})_{kl}$ coefficients and $\tilde{g} = \det(\mathbf{g})$ are determined from the rovibrational $\mathbf{g} \in \mathbb{R}^{(D+3) \times (D+3)}$ matrix, defined as follows,

$$g_{kl} = \sum_{i=1}^N m_i \mathbf{t}_{ik}^T \mathbf{t}_{il}; \quad k, l = 1, 2, \dots, D+3 \tag{2}$$

with

$$\mathbf{t}_{ik} = \frac{\partial \mathbf{r}_i}{\partial q_k}; \quad k, l = 1, 2, \dots, D \tag{3}$$

$$\mathbf{t}_{i,D+a} = \mathbf{e}_a \times \mathbf{r}_i; \quad a = 1(x), 2(y), 3(z), \tag{4}$$

where \mathbf{r}_i are the body-fixed Cartesian coordinates for the i -th atom and \mathbf{e}_a represent the body-fixed unit vectors.

In the CH₄–H₂O dimer, the intermolecular degrees of freedom ($D = 6$, Fig. 1) are defined with the following internal coordinates: the $R \in [0, \infty)$ distance between the centers of mass of the monomers; two angles, $\cos \theta \in [-1, 1]$ and $\phi \in [0, 2\pi)$, to

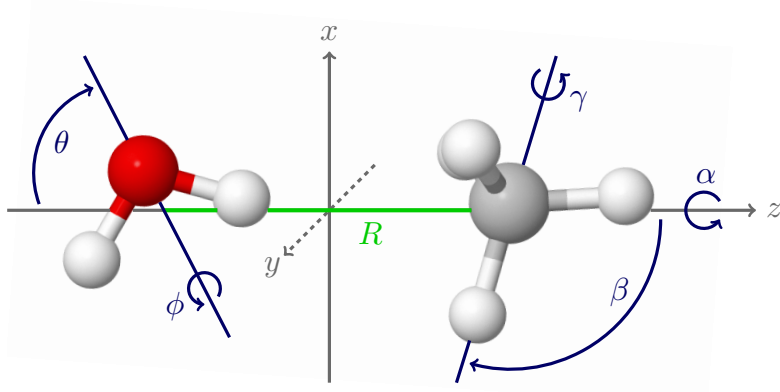


FIG. 1. Definition of the intermolecular coordinates, $(R, \theta, \phi, \alpha, \beta, \gamma)$ of the $\text{CH}_4\text{-H}_2\text{O}$ dimer.

describe the orientation of H_2O ; and three angles, $\alpha \in [0, 2\pi)$, $\cos \beta \in [-1, 1]$ and $\gamma \in [0, 2\pi)$, to describe the orientation of CH_4 . The monomer structures are fixed at the effective vibrational structures used for the development of the PES in Ref. [33] and in earlier rovibrational computations [24, 25]. For completeness, we repeat here the values of the constrained {bond length, angle} values, that are $\{r(\text{O-H}) = 0.9716257 \text{ \AA}, \alpha(\text{H-O-H}) = 104.69^\circ\}$ and $\{r(\text{C-H}) = 1.099122 \text{ \AA}, \cos \alpha(\text{H-C-H}) = -1/3\}$, for the water and the methane fragments, respectively. We used the same atomic masses as in Refs. [25] and [24]: $m(\text{H}) = 1.007825 m_u$, $m(\text{C}) = 12 m_u$ and $m(\text{O}) = 15.994915 m_u$. Since, we use the same PES, constrained coordinates, and nuclear (atomic) mass values as Ref. [24] (and also Ref. [25]) direct comparison of the results is possible.

In the present work, the matrix representation of the Hamiltonian is constructed using a direct product discrete variable representation (DVR) [42] for the vibrational degrees of freedom. For our curvilinear coordinate representation (Fig. 1), the KEO has singularities at $\cos \theta = \pm 1$ and $\cos \beta = \pm 1$. Plain Legendre DVR can be used for these coordinates, but the convergence of the (ro)vibrational energies is slow and an excessive number of grid points is needed even for a moderate level of convergence [25, 27, 38]. The representation is fundamentally correct, since we have repulsive singularities in the KEO Figure 2, but it is computationally inefficient. (We note that while in Fig. 2 both positive and negative singular values can be seen, the integrals are always positive.) This behaviour was correctly pointed out by Wang

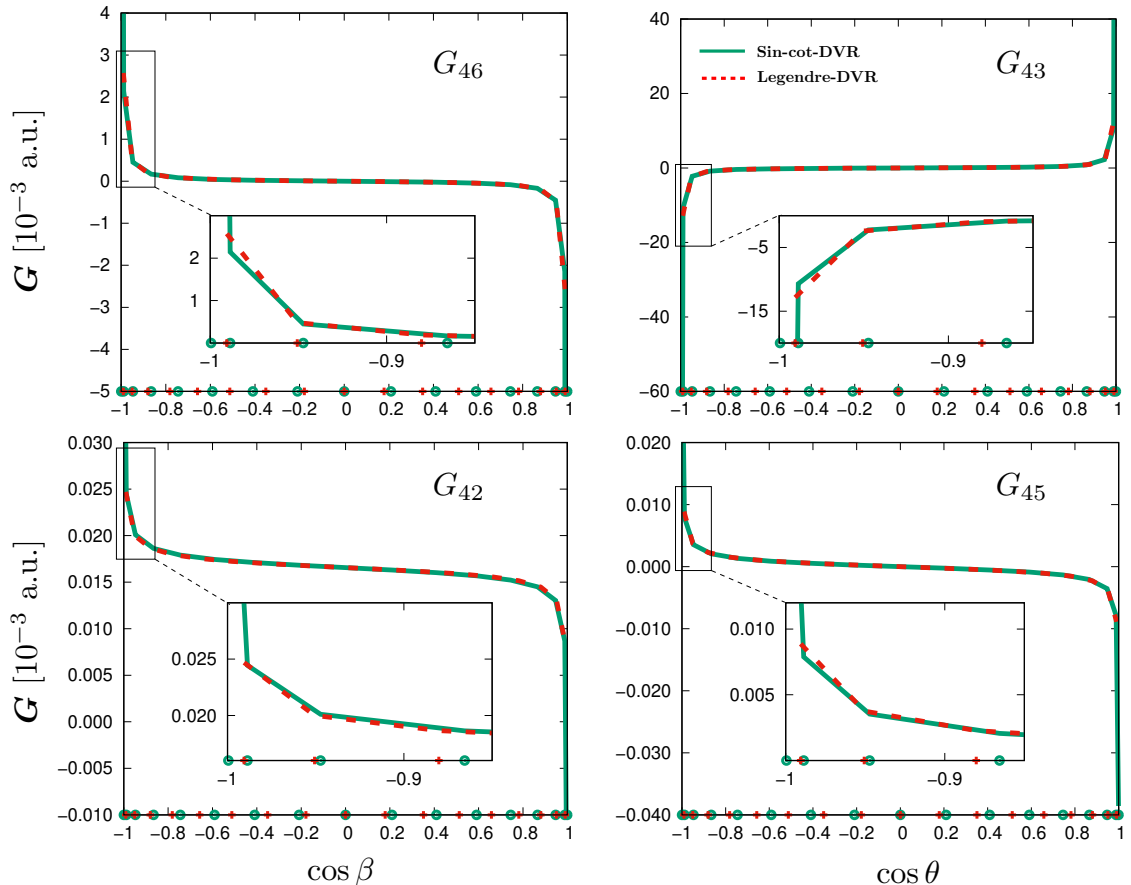


FIG. 2. Selected elements of the \mathbf{G} matrix shown along the singular coordinates, $\cos \beta$ and $\cos \theta$ (while all other coordinates are fixed). The Legendre and sine-cot-DVR grid points (17 of each) are plotted on the x axis of each subfigure. Both sets of points approach the ± 1 singular points, but the sine-cot-DVR points have a higher density near the singularities.

and Carrington in Ref. [24]. A direct product basis and grid with Legendre DVR used in the GENIUSH computations [25, 27, 38], which was 20 times larger than the coupled basis representation with Wigner D functions of Wang and Carrington [24], was sufficient to converge the rovibrational states in the ZPV splitting range only with a convergence error as large as 0.44 cm^{-1} and an erroneous split for some of the degenerate levels. At the same time, we note that this split did not hinder the unambiguous molecular symmetry group assignment of the GENIUSH results using the coupled-rotor decomposition scheme [26].

This convergence problem was intriguing for a full(12)-dimensional computation of the methane-argon complex studied by two of us [21]. In order to make the 12D

TABLE I. Coordinate intervals and representations used in the GENIUSH rovibrational computations.

Coord.	GM ^a	DVR		No. points
		type	interval	
R [Å]	3.464	PO-Laguerre ^b	[2.5,6.0]	15
θ [°]	116.190	Sine-Cot-DVR ^c	(0,180)	17
ϕ [°]	90.000	Fourier	[0,360]	15
α [°]	297.460	Fourier	[0,360]	9
β [°]	113.050	Sine-Cot-DVR ^c	(0,180)	17
γ [°]	293.010	Fourier	[0,360]	23

^a Internal coordinates values for the global minimum (GM) structure of the AOSz05 PES [33].

^b Potential-optimized DVR using 300 points.

^c $\cos \beta$ and $\cos \theta$ were the active coordinates and the sine-cot-DVR was constructed with two sine functions.

computation feasible, the more efficient, sine-cot-DVR developed by Schiffel and Manthe [43] was used for the singular coordinate (that was the second Euler angle in that system). The sine-cot-DVR was developed by Schiffel and Manthe [43] to have a more efficient representation of the quantum mechanical motion along the singular coordinate. (We note that the singularity is present only for $K \neq 0$ in the $|J, K\rangle$ basis representation of Ref. [43].) It uses a polynomial series of cosine, and optionally also sine, functions to build a DVR. In the present work, we obtained the best results when two sine functions were also included, and the ‘final’ computational parameters are summarized in Table I.

III. ENERGY LEVELS AND CONVERGENCE TESTS

First, the convergence of the results has been tested with respect to the number of grid points for every coordinate using a series of reduced-dimensional ($D < 6$) and full-dimensional ($D = 6$) computations. Table II highlights the 10^{-3} cm^{-1} convergence of the first 20 vibrational states for the selected grid parameters (Table I).

In Table II, we can observe a small, 10^{-3} cm^{-1} artificial split of some of the triply degenerate levels, which is due to the fact that the underlying grid and basis do not respect the full symmetry of the dimer, hence certain symmetry features are converged numerically by enlargement of the grid. At the same time, looking at this level of convergence, we felt important to check three additional computational parameters that are listed in the following paragraphs and summarized in Table III.

a. Testing the finite differences calculation of the vibrational t-vectors We have tested the accuracy of the vibrational t-vectors, the \mathbf{t}_{ik} vectors in Eq. (3) that are the derivatives of the body-fixed Cartesian coordinates with respect to the internal coordinates and are calculated in GENIUSH using finite differences. We have studied the effect of the ζ step size in the two-sided difference formula (that could have been meaningfully used also near the boundaries for the grid types listed in Table II). The default value for the step size is $\zeta = 10^{-5}$ a.u. [1], which we use in our original study, but we have performed computations also with $\zeta = 10^{-6}$ a.u. The ‘NumStep’ column of Table III shows that the effect of this change for the lowest twenty vibrational states is less than 10^{-5} cm^{-1} .

b. PES symmetrization Wang and Carrington [24] pointed out that there is a small imperfection in the AOSz05 PES [33] with respect to the (123) and (132) permutations of the methane protons, and for this reason they used a symmetrized version of the PES by averaging over the rotated geometries (perfect numerical symmetry was critical for them for using the symmetry-adapted Lanczos eigensolver). The ‘PESsym’ column of Table III shows that the effect of this operation is less than $3 \times 10^{-7} \text{ cm}^{-1}$.

c. Generation of the \mathbf{G} matrix over the grid points by increased precision computer algebra To check the numerical KEO procedure for this example, we generated the \mathbf{G} matrix values over the entire grid using the Wolfram Mathematica

TABLE II. Convergence test of the vibrational ($J = 0$) energy levels, in cm^{-1} , referenced to the zero-point vibrational energy in the methane-water dimer computed with the GENIUSH program and the AOSz05 PES [33].

$J0.n$	$\tilde{\nu}^a$	$\delta^{(-2)}^b$	$\delta^{(+2)}^c$
$N_b :$	$1.4 \cdot 10^7$	$5.6 \cdot 10^6$	$5.9 \cdot 10^7$
1	206.81	0.001	0
2	4.764	0.001	0
3	4.764	0.001	0
4	4.765	-0.001	0.001
5	6.992	0.002	0
6	11.25	0.002	0
7	11.251	0.003	0.001
8	11.251	0	0
9	29.033	-0.001	0
10	29.034	-0.001	0.001
11	29.034	-0.001	0
12	32.636	0.003	0
13	32.637	0	0
14	32.637	0	0
15	32.711	0.002	0
16	32.712	0.001	0.001
17	32.712	0.001	0
18	34.41	0	0
19	35.92	0	0
20	35.92	0	0

^a Obtained with the (15,17,15,9,17,23) grid documented in Table II.

^b $\delta^{(-2)} = \tilde{\nu} - \tilde{\nu}^{(-2)}$, where $\tilde{\nu}^{(-2)}$ was obtained with the same type of grid as in (a), but with fewer points: (13,15,13,9,15,21).

^c $\delta^{(+2)} = \tilde{\nu} - \tilde{\nu}^{(+2)}$, where $\tilde{\nu}^{(+2)}$ was obtained with the same type of grid as in (a), but with more points: (17,19,17,11,19,25).

symbolic algebra program [44] with 20 digits precision. Note that we use quadruple precision in the Fortran implementation of GENIUSH for the finite difference calculation of the vibrational t-vectors, but only double precision for the inversion of the \mathbf{g} matrix. Since near the singularities, we have to deal with small (large) values, and for this reason, we have decided to check the calculation procedure. The ‘CompAlg’ column of Table III shows that using an increased precision Mathematica calculation to generate all KEO coefficients has an effect smaller than 10^{-5} cm^{-1} on the first twenty vibrational states of methane-water.

TABLE III. Testing the computational setup in GENIUSH for the first twenty vibrational ($J = 0$) energy levels, in cm^{-1} , of MW and using the AOSz05 PES. The first energy value corresponds to the zero-point vibrational energy (ZPVE) and the other values are relative to the ZPVE.

$J0.n$	$\tilde{\nu}_0$	NumStep ^a	PESsym ^b	CompAlg ^c
1	206.81021	4×10^{-6}	1×10^{-8}	1×10^{-5}
2	4.76383	4×10^{-6}	3×10^{-7}	7×10^{-6}
3	4.76400	4×10^{-6}	3×10^{-7}	8×10^{-6}
4	4.76464	1×10^{-5}	3×10^{-8}	9×10^{-6}
5	6.99193	3×10^{-7}	2×10^{-8}	5×10^{-6}
6	11.25042	4×10^{-6}	3×10^{-7}	1×10^{-5}
7	11.25051	4×10^{-6}	4×10^{-7}	1×10^{-5}
8	11.25122	1×10^{-5}	1×10^{-8}	4×10^{-6}
9	29.03343	2×10^{-6}	6×10^{-8}	2×10^{-6}
10	29.03361	2×10^{-6}	5×10^{-8}	6×10^{-6}
11	29.03361	2×10^{-6}	7×10^{-8}	6×10^{-6}
12	32.63602	4×10^{-6}	3×10^{-8}	2×10^{-5}
13	32.63712	3×10^{-6}	2×10^{-7}	1×10^{-5}
14	32.63714	3×10^{-6}	1×10^{-7}	9×10^{-6}
15	32.71092	4×10^{-6}	2×10^{-8}	2×10^{-5}
16	32.7121	4×10^{-6}	2×10^{-7}	8×10^{-6}
17	32.7123	4×10^{-6}	2×10^{-7}	8×10^{-6}
18	34.41043	4×10^{-6}	6×10^{-8}	1×10^{-6}
19	35.91968	2×10^{-6}	2×10^{-8}	1×10^{-5}
20	35.91972	2×10^{-6}	2×10^{-8}	1×10^{-5}

^a $\tilde{\nu} - \tilde{\nu}_{\text{NumStep}}$, where $\tilde{\nu}_{\text{NumStep}}$ was obtained by changing the step size of the numerical finite difference calculation of the vibrational t-vectors in GENIUSH from $\zeta = 10^{-5}$ a.u. ($\tilde{\nu}_0$) to $\zeta = 10^{-6}$ a.u. (using quadruple precision in Fortran).

^b $\tilde{\nu} - \tilde{\nu}_{\text{PESsym}}$, where $\tilde{\nu}_{\text{PESsym}}$ was obtained by averaging for every PES points the effect of the identity and the (123) and (132) methane permutation.

^c $\tilde{\nu} - \tilde{\nu}_{\text{CompAlg}}$, where $\tilde{\nu}_{\text{CompAlg}}$ was obtained by generating the \mathbf{G} matrix elements using a Wolfram Mathematica implementation with 20 digits precision over the entire grid and performing the vibrational calculations with GENIUSH using these KEO coefficients.

IV. COMPARISON WITH WIGNER D BASIS FUNCTION COMPUTATIONS

The dimer Hamiltonian [7] used by Wang and Carrington in Ref. [24] corresponds to a different coordinate choice from ours. It relies on using two full sets of Euler angles (6 angles) to describe the monomers' rotation with respect to the dimer fixed frame (DF), and two additional angles are used to describe the rotational motion, while the separation of the centers of mass of the monomers is described with the R distance, similarly to our work. For this angular representation, the KEO can be written in terms of angular momentum operators and the kinetic energy matrix elements can be calculated analytically using Wigner's D functions [7]. The Wigner D functions are non-direct product functions, and they efficiently account for the singularities in the KEO. Wang and Carrington [24] combined this method with the Symmetry Adapted Lanczos (SAL) algorithm to obtain symmetry labels and to make their computations even more efficient.

Table IV presents the comparison of three approaches: a) the analytic dimer Hamiltonian and non-direct product Wigner D basis functions of Wang and Carrington [24]; b) GENIUSH with a numerical KEO and the 'smaller' direct-product grid using Legendre polynomials for the singular $\cos \theta$ and $\cos \beta$ coordinates of Ref. [25]; and c) the present GENIUSH computations with a numerical KEO and a direct-product grid in which the Legendre DVR is replaced with sine-cot-DVR for the singular coordinates.

By replacing the Legendre DVRs with sine-cot-DVRs, we can reduce the number of basis functions from 60 million (of the 'small' basis & grid [25]) to 13.4 million while the convergence from 'error' is reduced from $\sim 1 \text{ cm}^{-1}$ to 10^{-3} cm^{-1} . Our 'optimal' basis with 13.4 million functions are four-five times larger than the Wigner D basis including 2.97 million functions of Ref. [24], but we note that our smaller basis set with 6 million functions in Table II has an convergence error of only on the order of $\pm 3 \cdot 10^{-3} \text{ cm}^{-1}$. We also note that we observe a 0.02 cm^{-1} deviation between our 'optimal' basis results (Table IV) and results of Wang and Carrington [24] for the 36th vibrational state that can be assigned as the stretching fundamental. This convergence error reappears also for $J = 1$ (J1.86 in Table IV) that appears to be the

rotational excitation of the stretching fundamental vibration. Since we have carefully checked the convergence (and other computational parameters) in the present work, we think that this small difference in the energy list would probably disappear if Wang and Carrington [24] used a slightly larger basis set and grid along the R intermolecular stretching coordinate.

In our computations (DVR), the number of grid points equals the number of basis functions. Wang and Carrington reported only their basis set size, but we have not found any mention of the size of their grid (probably larger than the number of basis functions), while the grid size determines the computational cost (calculation of the matrix-vector product with the potential energy).

All in all, the agreement is remarkable, given the different coordinate representations, the entirely different KEOs and basis sets used to build the Hamiltonian matrix. We have not accounted for the symmetry, but the symmetry-adapted Lanczos algorithm can be used also in a GENIUSH computation [30]. The tailor-made, non-product Wigner D basis function computation remains to be the most efficient approach, but the numerical performance of the GENIUSH program (using the sine-cot-DVR of Schiffel and Manthe for the singular bending coordinates) becomes comparable to the specialized approach in terms of the basis set size and also in terms of the convergence of the energies.

TABLE IV. Comparison of a representative set of rovibrational energies referenced to the zero-point energy, in cm^{-1} , obtained with non-product (NP) and direct-product (DP) basis computations for the methane-water dimer. (The full list is provided in the SOM.)

Label	Sym. ^a	$\tilde{\nu}_{\text{NP}}$ [24] $3.0 \cdot 10^6$	$\tilde{\nu}'_{\text{DP}}$ [25] $6.0 \cdot 10^7$	$\tilde{\nu}_{\text{DP}}$ [This work] $1.4 \cdot 10^7$	$\tilde{\nu}_{\text{NP}} - \tilde{\nu}_{\text{DP}}$
J0.1	A ₁ ⁺	206.810	206.801	206.810	0.000
J0.2		4.765	4.763	4.764	0.001
J0.3	F ₂ ⁺	4.765	4.764	4.764	0.001
J0.4		4.765	4.764	4.765	0.000
J0.5	A ₂ ⁻	6.993	6.934	6.992	0.001
J0.18	A ₁ ⁺	34.413	34.405	34.410	0.003
J0.19	E ⁺	35.920	35.880	35.920	0.000
J0.20		35.920	35.880	35.920	0.000
J0.21	E ⁻	36.404	36.397	36.404	0.000
J0.22		36.404	36.397	36.405	0.000
J0.23		36.414	36.317	36.412	0.002
J0.24	F ₁ ⁺	36.414	36.317	36.413	0.001
J0.25		36.414	36.322	36.414	0.000
J0.36	A ₁ ⁺	48.706	48.685	48.686	0.020
J0.66	A ₂ ⁻	66.597	66.156	66.598	0.001
J1.1	A ₂ ⁺	0.289	0.289	0.289	0.000
J1.2		5.047	5.044	5.045	0.001
J1.3	F ₁ ⁺	5.047	5.044	5.046	0.001
J1.4		5.047	5.045	5.046	0.001
J1.5	A ₁ ⁻	7.282	7.219	7.281	0.001
J1.38		30.687	30.474	30.687	0.001
J1.39	F ₁ ⁺	30.687	30.474	30.687	0.001
J1.40		30.687	30.588	30.687	0.001
J1.41		30.688	30.588	30.687	0.001
J1.42	F ₂ ⁺	30.688	30.633	30.687	0.001
J1.43		30.688	30.633	30.687	0.001
J1.86	A ₂ ⁺	48.981	48.946	48.961	0.021

^a Symmetry labels corresponding to the character table of Wang and Carrington [24] instead of the table originally proposed by Dore et al. [28] used in Refs. [25, 26].

^b Number of basis functions that equals the number of grid points for the DP computations.

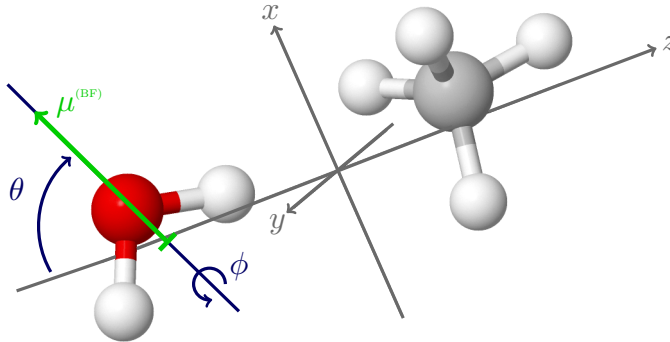


FIG. 3. Schematic representation of the dipole moment in the molecule-fixed frame of the $\text{CH}_4\text{-H}_2\text{O}$ dimer.

V. EVALUATION OF THE LINE STRENGTHS

Wang and Carrington [24] reported also line strength values for the rovibrational transitions using a simple but excellent model for the dimer's dipole moment. They set the dipole moment for the rigid water molecule to 1 (in arbitrary or 'normalized, relative' units), since the rigid methane fragment is apolar and does not contribute to this quantity. Using this dipole moment representation, they have computed the line strength for the rovibrational transitions and predicted that the global minimum to the secondary minimum transition should be well visible in the far infrared spectrum. The transition moment or line strength is defined by [45]

$$S(J'l' \leftarrow Jl) = g_{\text{ns}} \sum_{m,m'} \sum_{A=X,Y,Z} \left| \left\langle \Psi_{J'm'l'}^{(\text{rv})} \left| \mu_A \right| \Psi_{Jml}^{(\text{rv})} \right\rangle \right|^2, \quad (5)$$

where g_{ns} is the nuclear spin statistical weight factor and μ_A ($A = X, Y, Z$) are the components of the molecular dipole moment in the laboratory-fixed frame. The g_{ns} values have been calculated in Ref. [25]. We note that Ref. [24] reported the 'bare' values of the integrals (without the g_{ns} factor), that will be labelled as $S_0 = S/g_{\text{ns}}$ in the tables.

The rovibrational wave functions of the isolated molecule Hamiltonian, Eq. (1),

TABLE V. $U_{\omega\sigma,\alpha}^{(\Omega)}$ matrix elements for $\Omega = 1$.

(ω, σ)	α :	x	y	z
(1, -1)		$\frac{1}{\sqrt{2}}$	$-\frac{i}{\sqrt{2}}$	0
(1, 0)		0	0	1
(1, 1)		$-\frac{1}{\sqrt{2}}$	$-\frac{i}{\sqrt{2}}$	0

are represented in the GENIUSH program [34] as

$$\left| \Psi_{Jml}^{(\text{rv})} \right\rangle = \sum_{v=1}^{N_b} \sum_{k,\tau} c_{v,k,\tau}^{(Jl)} |v\rangle |J, k, m, \tau\rangle \quad (6)$$

expressed with the $|v\rangle$ vibrational wave function and the Wang-type symmetric top functions $|J, k, m, \tau\rangle = d_{+k}^{(\tau)} |J, k, m\rangle + d_{-k}^{(\tau)} |J, -k, m\rangle$.

Following Owens and Yachmenev, we evaluate the rovibrational integrals for Ω -order tensorial properties in the laboratory-fixed frame (LF) [46] as:

$$\left\langle \Psi_{J'm'l'}^{(\text{rv})} \left| T_A^{(\text{LF})} \right| \Psi_{Jml}^{(\text{rv})} \right\rangle = \sum_{\omega=0}^{\Omega} \mathcal{M}_{A\omega}^{(J'm',Jm)} \mathcal{K}_{\omega}^{(J'l',Jl)} \quad (7)$$

with

$$\mathcal{M}_{A\omega}^{(J'm',Jm)} = (-1)^{m'} \sqrt{(2J'+1)(2J+1)} \times \sum_{\sigma=-\omega}^{\omega} [U^{(\Omega)}]_{A,\omega\sigma}^{-1} \begin{pmatrix} J & \omega & J' \\ m & \sigma & -m' \end{pmatrix} \quad (8)$$

and

$$\begin{aligned} \mathcal{K}_{\omega}^{(J'l',Jl)} &= \sum_{\substack{v,k,\tau \\ v',k',\tau'}} [c_{v',k',\tau'}^{(J'l')}]^* c_{vk\tau}^{(Jl)} \sum_{\pm k', \pm k} [d_{k'}^{(\tau')}]^* d_k^{(\tau)} \\ &\times (-1)^{k'} \sum_{\sigma=-\omega}^{\omega} \sum_{\alpha} \begin{pmatrix} J & \omega & J' \\ k & \sigma & -k' \end{pmatrix} \times U_{\omega\sigma,\alpha}^{(\Omega)} \langle v' | T_{\alpha}^{(\text{BF})} | v \rangle. \end{aligned} \quad (9)$$

The electric dipole moment is a rank-1 tensor (a vector) with $\Omega = 1$, and the corresponding U matrix values are summarized in Table V. For higher-order tensor

operators, this matrix can be calculated from lower rank tensors using the following expression

$$U_{\omega\sigma,A}^{(\Omega)} = \sum_{\sigma_1=-\omega_1}^{\omega_1} \sum_{\sigma_2=-\omega_2}^{\omega_2} \langle \omega_1\sigma_1\omega_2\sigma_2|\omega\sigma \rangle U_{\omega_1\sigma_1,B}^{(\Omega_1)} U_{\omega_2\sigma_2,C}^{(\Omega_2)}, \quad (10)$$

where $\Omega = \Omega_1 + \Omega_2$, $A = B \otimes C$ and $\langle \omega_1\sigma_1\omega_2\sigma_2|\omega\sigma \rangle$ is the Clebsch–Gordan coefficient.

Regarding the transition dipoles of methane-water, we have first computed the vibrational matrix elements $\langle v' | \mu_\alpha^{(\text{BF})} | v \rangle$, using the H₂O dipole approximation of Ref. [24], *i.e.*, that only the water monomer contributes to the dipole moment of the dimer (Fig. 3). It is shown in the Figure that in our representation this dipole vector points along the Z axis of the H₂O monomer frame, and in the dimer’s frame its rotation is described with the θ and ϕ angles (although the value of ϕ is irrelevant in this special case). Hence, it was straightforward to implement this (presumably excellent) approximation for the body-(dimer-)fixed dipole moment $\mu_\alpha^{(\text{BF})}$. and calculate its value at a grid point in the body-fixed (dimer’s) frame, and then integrate it for pairs of vibrational eigenvectors.

VI. FAR INFRARED SPECTRUM

The rovibrational transitions computed in this work are compared in Tables VI–XIII with the transitions computed by Wang and Carrington [24] and with the transitions observed experimentally in the far-infrared range by Dore *et al.* [28]. In addition to the 13 experimentally observed vibration-rotation-tunnelling bands reported by Dore *et al.*: $(E)_1$, $(E)_2$, $(A/F)_1$, $(A/F)_2$, $(A/F)_3$ and $(A/F)_4$ for *ortho*-H₂O, $(E)_3$, $(E)_4$, $(E)_5$, $(A/F)_5$, $(A/F)_6$, $(A/F)_7$ and $(A/F)_8$ for *para*-H₂O; Wang and Carrington predicted 8 additional bands [24] (and of course computations can predict more): $(A/F)_{1b}$, $(A/F)_{3X}$, $(A/F)_{4X}$, $(A/F)_{5X}$, $(A/F)_{6X}$, $(A/F)_{6Y}$, $(A/F)_{8X}$ and $(A/F)_{8Y}$. The tables show that the two computations are in an excellent agreement. regarding the theory-experiment comparison, we reiterate the early observation [25], according to which the discrepancies are larger for the transitions including the *para*-H₂O than the *ortho*-H₂O species.

TABLE VI. $(E)_1$ and $(E)_2$ bands of the CH₄–H₂O. All transitions are reported in cm⁻¹ except where it is otherwise stated. $(J, n)'$ and (J, n) label the rovibrational state in our energy lists provided in the SOM. [this w]: [this work]. $\Delta\nu = E' - E$. S_0 is the line strength, Eq. (5), without the spin statistical weight factor [25].

$(J, n)' \leftarrow (J, n)$	$\Delta\tilde{\nu}_{\text{obs}}$ [MHz] [28]	$\Delta\tilde{\nu}_{\text{obs}}$	E' [this w]	E [this w]	$\Delta\tilde{\nu}$ [this w]	$\Delta\tilde{\nu}$ [24]	S_0 [this w]	S_0 [24]
Expt. [28]: Table III, $(E)_1$, $\Sigma \leftarrow \Pi$ band								
0, 21–22 \leftarrow 1, 23–24	532812.0	17.7727	36.4045	19.3909	17.0136	17.0099	0.155	0.154
1, 53–54 \leftarrow 1, 23–24	541359.5	18.0578	36.6889	19.3909	17.2980	17.2946	0.232	0.230
2, 75–76 \leftarrow 1, 23–24	558451.2	18.6279	37.2577	19.3909	17.8668	17.8638	0.074	0.073
1, 53–54 \leftarrow 2, 23–24	524254.1	17.4872	36.6889	19.9581	16.7309	16.7270	0.232	0.230
2, 75–76 \leftarrow 2, 23–24	541344.3	18.0573	37.2577	19.9581	17.2996	17.2962	0.393	0.391
Expt. [28]: Table III, $(E)_2$, $\Delta \leftarrow \Pi$ band								
2, 80–81 \leftarrow 2, 23–24	542744.8	18.1040	37.5721	19.9581	17.6140	17.6100	0.263	0.262
2, 80–81 \leftarrow 1, 23–24	559850.8	18.6746	37.5721	19.3909	18.1812	18.1800	0.484	0.482

TABLE VII. $(A/F)_1$ and $(A/F)_3$ bands of the $\text{CH}_4\text{-H}_2\text{O}$. See also caption to Table VI.

$(J, n)' \leftarrow (J, n)$	$\Delta\tilde{\nu}_{\text{obs}}$ [MHz] [28]	$\Delta\tilde{\nu}_{\text{obs}}$	E' [this w]	E [this w]	$\Delta\tilde{\nu}$ [this w]	$\Delta\tilde{\nu}$ [24]	S_0 [this w]	S_0 [24]
Expt. (Ref. [28]): Table IV, $(A/F)_1, \Sigma \leftarrow \Pi$ band								
0, 12–14 \leftarrow 1, 20–22	538189.8	17.9521	32.6368	14.6152	18.0215	18.0194	0.167	0.166
1, 47–49 \leftarrow 1, 20–22	546831.5	18.2403	33.0018	14.6152	18.3866	18.3839	0.231	0.230
2, 60–62 \leftarrow 1, 20–22	564291.7	18.8227	33.5026	14.6152	18.8874	18.8858	0.080	0.080
1, 47–49 \leftarrow 2, 17–19	529495.8	17.6621	33.0018	15.1903	17.8115	17.8083	0.234	0.232
2, 60–62 \leftarrow 2, 17–19	546715.2	18.2365	33.5026	15.1903	18.3123	18.3102	0.420	0.417
Predicted in Ref. [24]: $(A/F)_{1b}, \Delta \leftarrow \Pi$ band								
0, 15–17 \leftarrow 1, 17–19	–	–	32.7118	14.6124	18.0994	18.0960	0.155	0.154
1, 44–46 \leftarrow 1, 17–19	–	–	32.9254	14.6124	18.3130	18.3106	0.249	0.248
2, 63–65 \leftarrow 1, 17–19	–	–	33.5818	14.6124	18.9693	18.9667	0.076	0.076
1, 44–46 \leftarrow 2, 20–22	–	–	32.9254	15.1975	17.7279	17.7254	0.251	0.250
2, 63–65 \leftarrow 2, 20–22	–	–	33.5818	15.1975	18.3843	18.3815	0.387	0.384
Expt. (Ref. [28]): Table IV, $(A/F)_{3a}, \Delta \leftarrow \Pi$ band								
2, 66–71 ^a \leftarrow 2, 17–19	564637.3	18.8343	34.1923	15.1903	19.0020	18.9991	0.217	0.215
2, 66–71 ^a \leftarrow 1, 20–22	581971.4	19.4125	34.1923	14.6152	19.5770	19.5747	0.392	0.389
Expt. (Ref. [28]): Table IV, $(A/F)_{3b}, \Delta \leftarrow \Pi$ band								
2, 66–71 ^a \leftarrow 2, 20–22	564437.7	18.8276	34.1925	15.1975	18.9950	18.9919	0.218	0.217
2, 66–71 ^a \leftarrow 1, 17–19	582013.5	19.4139	34.1925	14.6124	19.5801	19.5771	0.391	0.388
Predicted in Ref. [24]: $(A/F)_{3Xa}, \Delta \leftarrow \Pi$ band								
2, 54–59 ^a \leftarrow 2, 17–19	–	–	32.8319	15.1903	17.6416	17.6405	0.040	0.040
2, 54–59 ^a \leftarrow 1, 20–22	–	–	32.8319	14.6152	18.2167	18.2161	0.075	0.075
Predicted in Ref. [24]: $(A/F)_{3Xb}, \Delta \leftarrow \Pi$ band								
2, 54–59 ^a \leftarrow 2, 20–22	–	–	32.8331	15.1975	17.6357	17.6333	0.042	0.042 ^b
2, 54–59 ^a \leftarrow 1, 17–19	–	–	32.8331	14.6124	18.2207	18.2185	0.074	0.074 ^b

^a Only three of the six upper states, which are very close in energy (and for this reason, listed together in our tables), give contribution to the S_0 line strength

^b: These two values are interchanged in Ref. [24].

TABLE VIII. $(A/F)_2$ band of the $\text{CH}_4\text{-H}_2\text{O}$. See also caption to Table VI.

$(J, n)' \leftarrow (J, n)$	$\Delta\tilde{\nu}_{\text{obs}}$ [MHz] [28]	$\Delta\tilde{\nu}_{\text{obs}}$	E' [this w]	E [this w]	$\Delta\tilde{\nu}$ [this w]	$\Delta\tilde{\nu}$ [24]	S_0 [this w]	S_0 [24]
Expt. (Ref. [28]): Table V, $(A/F)_2$, $\Pi \leftarrow \Sigma$ band								
1, 35–37 \leftarrow 0, 6–8	562445.5	18.7612	29.7641	11.2507	18.5134	18.5106	0.319	0.317
1, 32–34 \leftarrow 1, 12–14	553888.4	18.4757	29.7619	11.5324	18.2294	18.2265	0.480	0.477
1, 35–37 \leftarrow 2, 12–14	536931.0	17.9101	29.7641	12.0959	17.6682	17.6648	0.161	0.160
2, 45–47 \leftarrow 1, 12–14	571055.5	19.0484	30.3357	11.5324	18.8033	18.8009	0.477	0.475
2, 42–44 \leftarrow 2, 12–14	553883.6	18.4756	30.3291	12.0959	18.2332	18.2303	0.799	0.794

 TABLE IX. $(A/F)_4$ band of the $\text{CH}_4\text{-H}_2\text{O}$. See also caption to Table VI.

$(J, n)' \leftarrow (J, n)$	$\Delta\tilde{\nu}_{\text{obs}}$ [MHz] [28]	$\Delta\tilde{\nu}_{\text{obs}}$	E' [this w]	E [this w]	$\Delta\tilde{\nu}$ [this w]	$\Delta\tilde{\nu}$ [24]	S_0 [this w]	S_0 [24]
Expt. (Ref. [28]): Table VI, $(A/F)_4$, $\Pi \leftarrow \Sigma$ band								
1, 26 \leftarrow 0, 5	574574.9	19.1658	26.3646	6.9919	19.3727	19.3705	0.313	0.311
1, 25 \leftarrow 1, 5	565794.7	18.8729	26.3621	7.2805	19.0816	19.0792	0.473	0.471
1, 26 \leftarrow 2, 5	548506.7	18.2962	26.3646	7.8576	18.5070	18.5043	0.160	0.158
2, 34 \leftarrow 1, 5	583344.0	19.4583	26.9463	7.2805	19.6657	19.6638	0.467	0.464
2, 33 \leftarrow 2, 5	565694.1	18.8695	26.9386	7.8576	19.0810	19.0787	0.787	0.783
Predicted in Ref. [24]: $(A/F)_{4X}$, $\Pi \leftarrow \Sigma$ band								
1, 69 \leftarrow 0, 5	–	–	43.0625	6.9919	36.0706	36.0682	0.046	0.046
1, 70 \leftarrow 1, 5	–	–	43.0660	7.2805	35.7855	35.7829	0.071	0.071
1, 69 \leftarrow 2, 5	–	–	43.0625	7.8576	35.2049	35.2020	0.024	0.024
2, 101 \leftarrow 1, 5	–	–	43.6042	7.2805	36.3236	36.3213	0.068	0.068
2, 102 \leftarrow 2, 5	–	–	43.6147	7.8576	35.7571	35.7544	0.118	0.118

TABLE X. $(E)_3$, $(E)_4$ and $(E)_5$ bands of the $\text{CH}_4\text{-H}_2\text{O}$. See also caption to Table VI.

$(J, n)' \leftarrow (J, n)$	$\Delta\tilde{\nu}_{\text{obs}}$ [MHz] [28]	$\Delta\tilde{\nu}_{\text{obs}}$	E' [this w]	E [this w]	$\Delta\tilde{\nu}$ [this w]	$\Delta\tilde{\nu}$ [24]	S_0 [this w]	S_0 [24]
Expt. (Ref. [28]): Table VII, $(E)_3$, $\Sigma \leftarrow \Pi$ band								
0, 19–20 \leftarrow 1, 15–16	732385.1	24.4297	35.9197	13.1087	22.8110	22.8098	0.093	0.092
1, 51–52 \leftarrow 1, 15–16	740778.1	24.7097	36.1856	13.1087	23.0769	23.0757	0.141	0.140
1, 51–52 \leftarrow 2, 15–16	723657.8	24.1386	36.1856	13.6782	23.0769	22.5057	0.136	0.135
2, 73–74 \leftarrow 1, 15–16	757561.5	25.2695	36.7175	13.1087	23.6088	23.6078	0.048	0.048
2, 73–74 \leftarrow 2, 15–16	740443.2	24.6985	36.7175	13.6782	23.0393	23.0378	0.232	0.231
Expt. (Ref. [28]): Table VII, $(E)_4$, $\Sigma \leftarrow \Pi$ band								
2, 88–89 \leftarrow 2, 15–16	821483.9	27.4018	38.6481	13.6782	24.9700	24.9680	0.212	0.212
2, 88–89 \leftarrow 1, 15–16	838603.8	27.9728	38.6481	13.1087	25.5395	25.5380	0.396	0.394
Expt. (Ref. [28]): Table VII, $(E)'_4$, $\Sigma \leftarrow \Pi$ band								
2, 90–91 \leftarrow 2, 15–16	821483.9	27.4018	39.5975	13.6782	25.9193	25.9171	0.005	0.005
2, 90–91 \leftarrow 1, 15–16	838603.8	27.9728	39.5975	13.1087	26.4888	26.4871	0.001	0.001
1, 58–59* \leftarrow 2, 15–16	–	–	39.0170	13.6782	25.3388	25.3362 ^a	0.001	0.001
1, 58–59* \leftarrow 1, 15–16	–	–	39.0170	13.1087	25.9083	25.9062 ^a	0.001	0.001
Expt. (Ref. [28]): Table VII, $(E)_5$, $\Sigma \leftarrow \Pi$ band								
0, 34–35 \leftarrow 1, 15–16	–	–	48.0961	13.1087	34.9874	34.9863	0.088	0.087
1, 84–85 \leftarrow 1, 15–16	1057943.1	35.2892	48.3769	13.1087	35.2682	35.2673	0.132	0.132
2, 116–117 \leftarrow 1, 15–16	1074920.4	35.8555	48.9384	13.1087	35.8297	35.8292	0.044	0.044
2, 116–117 \leftarrow 2, 15–16	1057801.7	35.2845	48.9384	13.6782	35.2602	35.2592	0.221	0.219

^a We believe that there were some typos in Table XVIII in Ref. [24]. Corrected values and labels are given here in comparison with the values computed in this work.

TABLE XI. $(A/F)_5$ band of the $\text{CH}_4\text{-H}_2\text{O}$. See also caption to Table VI.

$(J, n)' \leftarrow (J, n)$	$\Delta\tilde{\nu}_{\text{obs}}$ [MHz]	$\Delta\tilde{\nu}_{\text{obs}}$	E'	E	$\Delta\tilde{\nu}$	$\Delta\tilde{\nu}$	S_0	S_0
	[28]		[this w]	[this w]	[this w]	[24]	[this w]	[24]
Expt. (Ref. [28]): Table VIII, $(A/F)_5$, $\Pi \leftarrow \Sigma$ band								
1, 38–40 \leftarrow 0, 2–4	852462.1	28.4351	30.6867	4.7642	25.9225	25.9223	0.256	0.255
1, 41–43 \leftarrow 1, 2–4	844268.9	28.1618	30.6873	5.0455	25.6417	25.6413	0.368	0.368
1, 38–40 \leftarrow 2, 2–4	827031.4	27.5868	30.6867	5.6083	25.0784	25.0774	0.114	0.113
2, 48–50 \leftarrow 1, 2–4	860602.5	28.7066	31.2548	5.0455	26.2093	26.2092	0.399	0.397
2, 51–53 \leftarrow 2, 2–4	844500.0	28.1695	31.2568	5.6083	25.6485	25.6479	0.615	0.612
$(A/F)_{5X}$, $\Pi \leftarrow \Sigma$ band								
1, 60–62 \leftarrow 0, 2–4	–	–	40.4210	4.7642	35.6569	35.6572	0.105	0.105
1, 63–64 \leftarrow 1, 2–4	–	–	40.4225	5.0455	35.3769	35.3770	0.164	0.164
1, 60–62 \leftarrow 2, 2–4	–	–	40.4210	5.6083	34.8127	34.8123	0.060	0.060
2, 92–94 \leftarrow 1, 2–4	–	–	40.9716	5.0455	35.9261	35.9267	0.150	0.150
2, 95–97 \leftarrow 2, 2–4	–	–	40.9761	5.6083	35.3678	35.3678	0.273	0.271

TABLE XII. $(A/F)_6$ and $(A/F)_7$ bands of the $\text{CH}_4\text{-H}_2\text{O}$. See also caption to Table VI.

$(J, n)' \leftarrow (J, n)$	$\Delta\tilde{\nu}_{\text{obs}}$ [MHz] [28]	$\Delta\tilde{\nu}_{\text{obs}}$	E' [this w]	E [this w]	$\Delta\tilde{\nu}$ [this w]	$\Delta\tilde{\nu}$ [24]	S_0 [this w]	S_0 [24]
Expt. (Ref. [28]): Table IX, $(A/F)_6$, $\Sigma \leftarrow \Pi$ band								
0, 23–25 \leftarrow 1, 6–8	–	–	36.4131	7.9119	28.5012	28.5020	0.181	0.180
1, 55–57 \leftarrow 1, 9–11	906722.4	30.2450	36.6984	7.9158	28.7826	28.7837	0.276	0.275
1, 55–57 \leftarrow 2, 6–8	889393.8	29.6670	36.6984	8.4916	28.2069	28.2075	0.265	0.264
2, 77–79 \leftarrow 1, 6–8	924003.8	30.8214	37.2689	7.9119	29.3570	29.3583	0.103	0.103
2, 77–79 \leftarrow 2, 9–11	906302.4	30.2310	37.2689	8.5026	28.7663	28.7672	0.446	0.444
Predicted in Ref. [24]: $(A/F)_{6X}$, $\Sigma \leftarrow \Pi$ band								
0, 9–11 \leftarrow 1, 9–11	–	–	29.0335	7.9158	21.1177	21.118	0.080	0.080
1, 27–29 \leftarrow 1, 6–8	–	–	29.3049	7.9119	21.3930	21.3563	0.117	0.117
1, 27–29 \leftarrow 2, 9–11	–	–	29.3049	8.5026	20.8023	20.8022	0.123	0.122
2, 37–39 \leftarrow 1, 9–11	–	–	29.8476	7.9158	21.9318	21.9325	0.038	0.037
2, 37–39 \leftarrow 2, 6–8	–	–	29.8476	8.4916	21.3560	21.3563	0.194	0.193
Predicted in Ref. [24]: $(A/F)_{6Y}$, $\Sigma \leftarrow \Pi$ band								
0, 26–28 \leftarrow 1, 9–11	–	–	41.1844	7.9158	33.2686	33.2700	0.101	0.100
1, 66–68 \leftarrow 1, 6–8	–	–	41.4639	7.9119	33.5520	33.5535 ^a	0.157	0.156
1, 66–68 \leftarrow 2, 9–11	–	–	41.4639	8.5026	32.9613	32.9624	0.147	0.147
2, 98–100 \leftarrow 1, 9–11	–	–	42.0229	7.9158	34.1071	34.1092	0.055	0.055
2, 98–100 \leftarrow 2, 6–8	–	–	42.229	8.4916	33.5313	33.5330	0.262	0.261
Expt. (Ref. [28]): Table IX, $(A/F)_{7a}$, $\Sigma \leftarrow \Pi$ band								
2, 82–87 ^b \leftarrow 2, 6–8	912803.3	30.4478	37.6439	8.4916	29.1523	29.1532	0.299	0.297
2, 82–87 ^b \leftarrow 1, 9–11	930130.4	31.0258	37.6439	7.9158	29.7281	29.7294	0.536	0.533
Expt. (Ref. [28]): Table IX, $(A/F)_{7b}$, $\Sigma \leftarrow \Pi$ band								
2, 82–87 ^b \leftarrow 2, 9–11	912529.1	30.4387	37.6447	8.5026	29.1421	29.1421	0.309	0.307
2, 82–87 ^b \leftarrow 1, 6–8	930230.6	31.0292	37.6447	7.9119	29.7328	29.7332	0.530	0.527

^a A typo in Table XX of Ref. [24] is corrected based on the E' and E'' level energies given in the paper and checked against results of this work.

^b See footnote *a* to Table VII.

TABLE XIII. $(A/F)_8$ band of the $\text{CH}_4\text{-H}_2\text{O}$. See also caption to Table VI.

$(J, n)' \leftarrow (J, n)$	$\Delta\tilde{\nu}_{\text{obs}}$ [MHz]	$\Delta\tilde{\nu}_{\text{obs}}$	E'	E	$\Delta\tilde{\nu}$	$\Delta\tilde{\nu}$	S_0	S_0
	[28]		[this w]	[this w]	[this w]	[24]	[this w]	[24]
Expt. (Ref. [28]): $(A/F)_8$, $\Pi \leftarrow \Sigma$ band								
1, 30 \leftarrow 0, 1	927673.3	30.9439	29.5588	0.0000	29.5588	29.5596	0.374	0.372
1, 31 \leftarrow 1, 1	919166.0	30.6601	29.5646	0.2891	29.2755	29.2762	0.554	0.551
1, 30 \leftarrow 2, 1	901595.6	30.0740	29.5588	0.8673	28.6915	28.6918	0.179	0.178
2, 40 \leftarrow 1, 1	936059.3	31.2236	30.1269	0.2891	29.8377	29.5596	0.569	0.566
2, 41 \leftarrow 2, 1	919232.4	30.6623	30.1444	0.8673	29.2771	29.2777	0.922	0.918
Predicted in Ref. [24]: $(A/F)_{8X}$, $\Pi \leftarrow \Sigma$ band								
0, 18 \leftarrow 1, 1	–	–	34.4104	0.2891	34.1213	34.1234	0.048	0.048
1, 50 \leftarrow 0, 1	–	–	34.6785	0.0000	34.6785	34.6811	0.046	0.046
1, 50 \leftarrow 2, 1	–	–	34.6785	0.8673	34.3894	33.8133	0.097	0.096
2, 72 \leftarrow 1, 1	–	–	35.2146	0.2891	34.9254	34.9283	0.091	0.090
Predicted in Ref. [24]: $(A/F)_{8Y}$, $\Pi \leftarrow \Sigma$ band								
0, 36 \leftarrow 1, 1	–	–	48.6856	0.2891	48.3965	48.4168	0.029	0.029
1, 86 \leftarrow 0, 1	–	–	48.9607	0.0000	48.9607	48.9812	0.027	0.027
1, 86 \leftarrow 2, 1	–	–	48.9607	0.8673	48.0934	48.1134	0.061	0.061
2, 118 \leftarrow 1, 1	–	–	49.5105	0.2891	49.2214	49.2419	0.052	0.052

VII. MICROWAVE SPECTRUM

Similarly to the far-infrared high-resolution spectroscopy experiments, comparison can be made (Table XIV) with microwave observations by Suenram *et al.* [29]. In the microwave spectrum, there were four Σ and six Π bands observed at $\sim 1K$ rotational temperature in the supersonic expansion. There is an excellent agreement with the experimental and also with the computed transitions by Wang and Carrington [24].

TABLE XIV. Rotation-vibration-tunneling transitions of CH₄-H₂O observed in microwave spectroscopy experiments [29]. See also caption to Table VI.

$(J, n)' \leftarrow (J, n)$	$\Delta\tilde{\nu}_{\text{obs}}$ [MHz] [28]	$\Delta\tilde{\nu}_{\text{obs}}$	E' [this w]	E [this w]	$\Delta\tilde{\nu}$ [this w]	$\Delta\tilde{\nu}$ [24]	S_0 [this w]	S_0 [24]
<i>A</i> ⁺ , Σ band:								
1, 1 \leftarrow 0, 1	8692.96	0.2900	0.2891	0.0000	0.2891	0.2893	0.040	0.040
2, 1 \leftarrow 1, 1	17383.1	0.5798	0.8673	0.2891	0.5781	0.5785	0.079	0.079
<i>F</i> ⁻ , Σ band:								
1, 12-14 \leftarrow 0, 6-8	8504.65	0.2837	11.5324	11.2507	0.2817	0.2819	0.029	0.029
2, 12-14 \leftarrow 1, 12-14	17007.9	0.567	12.0959	11.5324	0.5634	0.5639	0.059	0.059
<i>F</i> ⁺ , Σ band:								
1, 2-4 \leftarrow 0, 2-4	8476.93	0.2828	5.0455	4.7642	0.2814	0.2816	0.055	0.055
2, 2-4 \leftarrow 1, 2-4	16953.0	0.5655	5.6083	5.0455	0.5628	0.5632	0.109	0.109
<i>A</i> ⁻ , Σ band:								
1, 5 \leftarrow 0, 5	8690.39	0.2899	7.2805	6.9919	0.2886	0.2888	0.024	0.024
2, 5 \leftarrow 1, 5	17378.1	0.5797	7.8576	7.2805	0.5771	0.5774	0.048	0.048
<i>E</i> ⁺ , Π band:								
2, 15-16 \leftarrow 1, 15-16	17120.06	0.5711	13.6782	13.1087	0.5695	0.5700	0.099	0.099
<i>E</i> ⁻ , Π band:								
2, 23-24 \leftarrow 1, 23-24	17105.28	0.5706	19.9581	19.3909	0.5671	0.5676	0.052	0.052
<i>F</i> ⁺ , Π band:								
2, 6-8 \leftarrow 1, 6-8	17421.68	0.5811	8.4916	7.9119	0.5797	0.5800	0.072	0.071
2, 9-11 \leftarrow 1, 9-11	17607.7	0.5873	8.5026	7.9158	0.5868	0.5873	0.072	0.071
<i>F</i> ⁻ , Π band:								
2, 17-19 \leftarrow 1, 17-19	17396.81	0.5803	15.1903	14.6124	0.5779	0.5780	0.040	0.040
2, 20-22 \leftarrow 1, 20-22	17516.8	0.5843	15.1975	14.6152	0.5823	0.5828	0.040	0.040

VIII. SUMMARY, CONCLUSION, AND OUTLOOK

The black-box-type rovibrational method implemented in the GENIUSH program package has been extensively tested with respect to the sophisticated dimer Hamiltonian approach that has been tailored for describing the intermolecular dynamics of floppy dimers by Wang and Carrington [24].

GENIUSH uses a numerical kinetic energy operator approach, user-defined coordinates and body-fixed frame, and a direct product basis and grid. The dimer approach of Wang and Carrington uses an analytic kinetic energy operator, (non-direct product) coupled basis functions including Wigner’s D functions, and analytic kinetic energy operator matrix elements.

We show for the example of the rovibrational states and transitions of the methane-water dimer that the performance of the black-box-type approach is on the same order of magnitude as that of the tailor-made approach, the latter being more efficient. In our direct-product approach, it is important to use the sine-cot-DVR developed by Schiffel and Manthe [43] for the singular ‘bending’ coordinates. Then, we can converge the energy levels on the order of 10^{-3} cm^{-1} with a basis set only twice as large as the non-product dimer basis of Wang and Carrington [24]. (While our grid size is the same as our basis size, their grid size is unknown to us—most likely larger than their basis set size—that is the bottleneck of matrix-vector computations.) The well-converged data allowed us to spot that they should have used a slightly larger basis (and/or grid) for the intermolecular stretching degree of freedom, because they have an error of 0.02 cm^{-1} in the intermolecular stretching fundamental vibration energy.

To compute rovibrational transitions for $J = 0, 1,$ and 2 rotational quantum numbers, we use a basis set that is ca. 4.5 times as large as the non-product dimer basis of Wang and Carrington, and we evaluate rovibrational transition energies and line strengths. Our transition energies are in an agreement of 10^{-3} cm^{-1} often just a few 10^{-4} cm^{-1} of the energies reported by Wang and Carrington. These deviations are far beyond the theoretical uncertainty of the current rovibrational theoretical framework based on the non-relativistic and the Born–Oppenheimer approximations.

Regarding, further progress that we would be happy to witness in the forthcoming

years, is related to computing extensive line lists for floppy systems. An extensive line list—that can be useful for simulating molecular interactions [46] or providing datasets [47] to other disciplines—includes rotational excitations up to $J = 20$ and beyond. If we have to solve the the full rovibrational problem (from scratch) for every J , then a factor of 2-3-5 in the vibrational basis can be an important advantage (of the tailor-made method). A more efficient approach would be, however, if we had an method for finding a good body-fixed frame that allows one to use efficiently the knowledge of the solution of the $J = 0$ problem, the vibrational eigenstates in the energy range relevant for the dynamics. It may be the numerical KEO approach (also implemented in GENIUSH) that may allow the optimization of the body-fixed frame even for floppy systems [32].

All data that support findings of this study are included in the paper and in the Supplementary Material.

IX. ACKNOWLEDGMENT

We thank the financial support of the Swiss National Science Foundation (PROMYS Grant, No. IZ11Z0_166525). We are grateful to Xiao-Gang Wang and Tucker Carrington for the thorough documentation of their work in Ref. [24] and for paying attention to using exactly the same constant parameters as in Ref. [25] that made it possible for us to extensively test and further develop our methodologies. We also thank them for sharing their sine-cot-DVR implementation during our earlier work [21] that allowed us to test our computations also used in the present work.

-
- [1] E. Mátyus, G. Czakó, and A. G. Császár, Toward black-box-type full- and reduced-dimensional variational (ro)vibrational computations, *J. Chem. Phys.* **130**, 134112 (2009).
 - [2] R. Meyer and H. H. Günthard, Internal rotation and vibration in $\text{CH}_2=\text{CCl}-\text{CH}_2\text{D}$, *J. Chem. Phys.* **50**, 353 (1969).

- [3] D. Luckhaus, 6D vibrational quantum dynamics: Generalized coordinate discrete variable representation and (a)diabatic contraction, *J. Chem. Phys.* **113**, 1329 (2000).
- [4] D. Luckhaus, The vibrational spectrum of HONO: Fully coupled 6D direct dynamics, *J. Chem. Phys.* **118**, 8797 (2003).
- [5] D. Lauvergnat and A. Nauts, Exact numerical computation of a kinetic energy operator in curvilinear coordinates, *J. Chem. Phys.* **116**, 8560 (2002).
- [6] S. N. Yurchenko, W. Thiel, and P. Jensen, Theoretical ROVibrational Energies (TROVE): A robust numerical approach to the calculation of rovibrational energies for polyatomic molecules, *J. Mol. Spectrosc.* **245**, 126 (2007).
- [7] G. Brocks, A. van der Avoird, B. T. Sutcliffe, and J. Tennyson, Quantum dynamics of non-rigid systems comprising two polyatomic fragments, *Mol. Phys.* **50**, 1025 (1983).
- [8] Z. Bačić and J. C. Light, Theoretical methods for rovibrational states of floppy molecules, *Annu. Rev. Phys. Chem.* **40**, 469 (1989).
- [9] B. T. Sutcliffe and J. Tennyson, A general treatment of vibration-rotation coordinates for triatomic molecules, *Int. J. Quant. Chem.* **39**, 183 (1991).
- [10] M. J. Bramley and T. Carrington, Jr., A general discrete variable method to calculate vibrational energy levels of three- and four-atom molecules, *J. Chem. Phys.* **99**, 8519 (1994).
- [11] C. Leforestier, Grid method for the Wigner functions. application to the van der Waals system Ar-H₂O, *J. Chem. Phys.* **101**, 7357 (1994).
- [12] S. C. Althorpe and D. C. Clary, Calculation of the intermolecular bound states for water dimer, *J. Chem. Phys.* **101**, 3603 (1994).
- [13] D. H. Zhang, Q. Wu, J. Z. H. Zhang, M. von Dirke, and Z. Bačić, Exact full-dimensional bound state calculations for (HF)₂, (DF)₂, and HFDF, *J. Chem. Phys.* **102**, 2315 (1995).
- [14] M. Mladenović, Discrete variable approaches to tetratomic molecules: Part I: DVR(6) and DVR(3)+DGB methods, *Spectrochim. Acta* **58**, 795 (2002).
- [15] X.-G. Wang and T. Carrington, Jr., Contracted basis Lanczos methods for computing numerically exact rovibrational levels of methane, *J. Chem. Phys.* **121**, 2937 (2004).
- [16] J. K. G. Watson, Simplification of the molecular vibration-rotation hamiltonian, *Mol. Phys.* **15**, 479 (1968).

- [17] R. J. Whitehead and N. C. Handy, Variational calculation of vibration-rotation energy levels for triatomic molecules, *J. Mol. Spectrosc.* **55**, 356 (1975).
- [18] J. M. Bowman, S. Carter, and X. Huang, Multimode: A code to calculate rovibrational energies of polyatomic molecules, *Int. Rev. Phys. Chem.* **22**, 533 (2003).
- [19] G. Avila and J. T. Carrington, Nonproduct quadrature grids for solving the vibrational Schrödinger equation, *J. Chem. Phys.* **131**, 174103 (2009).
- [20] G. Avila and J. T. Carrington, Using nonproduct quadrature grids to solve the vibrational Schrödinger equation in 12D, *J. Chem. Phys.* **134**, 054126 (2011).
- [21] G. Avila and E. Mátyus, Toward breaking the curse of dimensionality in (ro)vibrational computations of molecular systems with multiple large-amplitude motions, *J. Chem. Phys.* **150**, 174107 (2019).
- [22] G. Avila and E. Mátyus, Full-dimensional (12D) variational vibrational states of $\text{CH}_4\cdot\text{F}^-$: interplay of anharmonicity and tunneling, *J. Chem. Phys.* **151**, 154301 (2019).
- [23] G. Avila, D. Papp, G. Czakó, and E. Mátyus, Exact quantum dynamics background of dispersion interactions: case study for $\text{CH}_4\cdot\text{Ar}$ in full (12) dimensions, *Phys. Chem. Chem. Phys.* **22**, 2792 (2020).
- [24] X.-G. Wang and J. T. Carrington, Using nondirect product Wigner D basis functions and the symmetry adapted lanczos algorithm to compute the ro-vibrational spectrum of $\text{CH}_4\text{-H}_2\text{O}$, *J. Chem. Phys.* **154**, 124112 (2021).
- [25] J. Sarka, A. G. Császár, S. C. Althorpe, D. J. Wales, and E. Mátyus, Rovibrational transitions of the methane-water dimer from intermolecular quantum dynamical computations, *Phys. Chem. Chem. Phys.* **18**, 22816 (2016).
- [26] J. Sarka, A. G. Császár, and E. Mátyus, Rovibrational quantum dynamical computations for deuterated isotopologues of the methane-water dimer, *Phys. Chem. Chem. Phys.* **19**, 15335 (2017).
- [27] M. P. Metz, K. Szalewicz, J. Sarka, R. Tóbiás, A. G. Császár, and E. Mátyus, Molecular dimers of methane clathrates: ab initio potential energy surfaces and variational vibrational states, *Phys. Chem. Chem. Phys.* **21**, 13504 (2019).
- [28] L. Dore, R. C. Cohen, C. A. Schmuttenmaer, K. L. Busarow, M. J. Elrod, J. G. Loeser, and R. J. Saykally, Far infrared vibration-rotation-tunneling spectroscopy and

- internal dynamics of methane-water: A prototypical hydrophobic system, *J. Chem. Phys.* **100**, 863 (1994).
- [29] R. D. Suenram, G. T. Fraser, F. J. Lovas, and Y. Kawashima, The microwave spectrum of $\text{CH}_4\text{-H}_2\text{O}$, journal = jcp, volume = 101, pages = 7230, year = 1994, doi= 10.1063/1.468280, .
- [30] C. Fábri, M. Quack, and A. G. Császár, On the use of nonrigid-molecular symmetry in nuclear motion computations employing a discrete variable representation: A case study of the bending energy levels of CH_5^+ , *J. Chem. Phys.* **147**, 134101 (2017).
- [31] E. Mátyus, C. Fábri, T. Szidarovszky, G. Czakó, W. D. Allen, and A. G. Császár, Assigning quantum labels to variationally computed rotational-vibrational eigenstates of polyatomic molecules, *J. Chem. Phys.* **133**, 034113 (2010).
- [32] G. Avila, A. Martín Santa Daría, and E. Mátyus, Optimization of the body-fixed frame to minimize rovibrational coupling, in preparation (2021).
- [33] O. Akin-Ojo and K. Szalewicz, Potential energy surface and second virial coefficient of methane-water from ab initio calculations, *J. Chem. Phys.* **123**, 134311 (2005).
- [34] C. Fábri, E. Mátyus, and A. G. Császár, Rotating full- and reduced-dimensional quantum chemical models of molecules, *J. Chem. Phys.* **134**, 074105 (2011).
- [35] C. Fábri, A. G. Császár, and G. Czakó, Reduced-dimensional quantum computations for the rotational-vibrational dynamics of f-ch4 and f-ch2d2, *J. Phys. Chem. A* **117**, 6975 (2013).
- [36] C. Fábri, E. Mátyus, and A. G. Császár, *Spectrochim. Acta* **119**, 84 (2014).
- [37] D. Papp, J. Sarka, T. Szidarovszky, A. G. Császár, E. Mátyus, M. Hochlaf, and T. Stoecklin, Complex rovibrational dynamics of the ar-no⁺ complex, *Phys. Chem. Chem. Phys.* **19**, 8152 (2017).
- [38] J. Sarka and A. G. Császár, Interpretation of the vibrational energy level structure of the astructural molecular ion H_5^+ and all of its deuterated isotopomers, *J. Chem. Phys.* **144**, 154309 (2016).
- [39] D. Ferenc and E. Mátyus, Bound and unbound rovibrational states of the methane-argon dimer, **117**, 1694 (2019).
- [40] G. A. A. Martín Santa Daría and E. Mátyus, Fingerprint region of the formic acid dimer: variational vibrational computations in curvilinear coordinates, *Phys. Chem.*

- Chem. Phys.* **23**, 6526 (2021).
- [41] R. Meyer, Flexible models for intramolecular motion, a versatile treatment and its application to glyoxal, *J. Mol. Spectrosc.* **76**, 266 (1979).
- [42] J. C. Light and T. Carrington Jr, Discrete variable representations and their utilization, *Adv. Chem. Phys.* **114**, 263 (2000).
- [43] G. Schiffel and U. Manthe, On direct product based discrete variable representations for angular coordinates and the treatment of singular terms in the kinetic energy operator, *Chem. Phys.* **374**, 118 (2010).
- [44] Wolfram Research, Inc., Mathematica, Version 12.1, Champaign, IL, 2020.
- [45] S. N. Yurchenko, R. J. Barber, A. Yachmenev, W. Thiel, P. Jensen, and J. Tennyson, A variationally computed $T = 300$ K line list for NH_3 , *J. Phys. Chem. A* **113**, 11845 (2009).
- [46] A. Owens and A. Yachmenev, Richmol: A general variational approach for rovibrational molecular dynamics in external electric fields, *J. Chem. Phys.* **148**, 124102 (2018).
- [47] J. Tennyson, S. N. Yurchenko, A. F. Al-Refaie, E. J. Barton, K. L. Chubb, P. A. Coles, S. Diamantopoulou, M. N. Gorman, C. Hill, A. Z. Lam, L. Lodi, L. K. McKemmish, Y. Na, A. Owens, O. L. Polyansky, T. Rivlin, C. Sousa-Silva, D. S. Underwood, A. Yachmenev, and E. Zak, The exomol database: Molecular line lists for exoplanet and other hot atmospheres, *Journal of Molecular Spectroscopy* **327**, 73 (2016), new Visions of Spectroscopic Databases, Volume II.